STREAMLINE CURVATURE AND CROSSFLOW EFFECTS ON THE TURBULENT BOUNDARY LAYER OVER A GAUSSIAN BUMP

Nicholas Morse[1]
[1]FLOW, Department of Engineering Mechanics
KTH Royal Institute of Technology
100 44 Stockholm, Sweden
morse@kth.se

Ronith Stanly[1]
[1]FLOW, Department of Engineering Mechanics
KTH Royal Institute of Technology
100 44 Stockholm, Sweden
ronith@kth.se

Ramis Örlü[1,2]
[2]Dept. of Mechanical, Electrical and Chemical Eng.
OsloMet – Oslo Metropolitan University
0166 Oslo, Norway
ramis.orlu@oslomet.no

Philipp Schlatter[1,3]
[3]Institute of Fluid Mechanics (LSTM)
Friedrich–Alexander–Universität (FAU)
91058 Erlangen, Germany
philipp.schlatter@fau.de

ABSTRACT

We perform direct numerical simulations (DNS) of the flow over the Boeing Gaussian bump in two configurations: the straight-ahead flow considered in published DNS, and in a 45° swept configuration, at the same bump Reynolds number of $Re_L = 1$ million. In the baseline (unswept) configuration, we analyze the flow in the streamline coordinate system to illustrate the direct and indirect curvature effects on the mean momentum balance and turbulence budgets. The swept flow exhibits much stronger separation on the leeward side of the bump than the baseline configuration, arising from the crossflow induced by the pressure gradients imposed by the bump.

INTRODUCTION

Turbulent boundary layers (TBLs) in engineering applications are often subject to pressure gradients and curvature effects (e.g. on wings, turbine blades, and ship hulls). While direct numerical simulations (DNS) and experiments have resulted in a mature understanding of zero-pressure-gradient (ZPG) flat-plate turbulent boundary layers (TBLs), the understanding of adverse/favorable pressure gradient (APG/FPG) TBLs is less developed, and even more so for curved boundary layers. The understanding of these more complex TBLs is further complicated for three-dimensional TBLs (3DTBLs), which exhibit a 3D mean flow via a “secondary” velocity superimposed on the primary flow, induced by either pressure gradient or viscous effects (Lozano-Durán et al., 2020).

The Boeing Gaussian bump (Slotnick, 2019) is a simplified geometry aiming to elicit the curvature, pressure gradient, and separation behavior of a TBL initially developing on a flat plate. The bump has a width L with error-function shoulders, and a centerline surface height described by a Gaussian function $y(x) = h\exp\left(-(x/a)^2\right)$, where $h/L = 0.085$ and $a/L = 0.195$. The incoming TBL experiences a mild adverse pressure gradient (APG) upstream of the bump, a favorable pressure gradient (FPG) approaching the bump apex, and a strong APG on the leeward side, with a corresponding concave–convex–concave evolution of streamline curvature.

The Boeing bump has been extensively studied through DNS of its planar center section, which has been conducted at Reynolds numbers based on L of $Re_L = 1$ million (Balin and Jansen, 2021; Uzun and Malik, 2021; Shur et al., 2021), 2 million (Uzun and Malik, 2022; Prakash et al., 2024), and up to 4 million (Uzun and Malik, 2025). At $Re_L = 1$ million, the leeward side of the bump experiences mild, incipient separation, which counterintuitively becomes more severe at higher Reynolds numbers. This behavior is linked to the partial relaminarization of the TBL in the FPG on the windward side of the bump (Uzun and Malik, 2021; Balin and Jansen, 2021), which re-transitions downstream of the bump apex, increasing momentum transfer to the wall (Uzun and Malik, 2022).

The rich phenomena observed for $Re_L = 1$ million motivate the present study, which expands on the existing literature on two fronts. First, details of the flow are explored in the streamline coordinate system (SCS) proposed by Finnigan (1983), which was recently used by Morse and Mahesh (2021) and Prakash et al. (2024) to study an axisymmetric TBL and the TBL on windward side of the bump at $Re_L = 2$ million, respectively. While these two studies focused on the contribution of streamwise curvature to the mean momentum balance of their respective TBLs, in the present work we take advantage of the SCS to investigate the role curvature plays in the Reynolds shear stress and turbulent kinetic energy budgets.

In the present study, we perform two new DNS of the bump at $Re_L = 1$ million: one corresponding to the unswept (baseline) configuration considered in past work, and another DNS at a sweep angle of $\Lambda = 45°$. For the baseline configuration, we examine the curvature contribution to the relaminarization region of the bump using the SCS. Then we examine the separation behavior of the 3DTBL for the swept configuration and discuss how the global flow features differ from the baseline case.

SIMULATION DETAILS

DNS is performed using the open-source spectral element solver *Nek5000* (Fischer et al., 2008) to advance the incompressible Navier–Stokes equations

$$\frac{\partial u_i}{\partial x_i} = 0\,,$$
$$\frac{\partial u_i}{\partial t} + u_j \frac{\partial u_i}{\partial x_j} = -\frac{\partial p}{\partial x_i} + \frac{1}{Re}\frac{\partial^2 u_i}{\partial x_j \partial x_j}\,, \tag{1}$$

where Re is the simulation Reynolds number.

The computational domain is a planar section along the centerline of the Boeing bump, in which the bump is centered at $x/L = 0$, as shown in figure 1. A no-slip condition is applied on the bottom wall, whose shape is described by the Gaussian function given in the introduction, while periodic boundary conditions are applied in the spanwise direction, which is of width $0.04L$, matching previous DNS (Uzun and Malik, 2021; Shur et al., 2021; Balin and Jansen, 2021). The domain extends to a stabilized outflow boundary at $x/L = 1$ downstream of the bump apex and upstream to the inlet, located at $x/L = -0.72$. At the inflow boundary, the time-dependent velocity field from a precursor simulation is specified as a Dirichlet condition, which is rotated by the sweep angle $\Lambda = 0^\circ$ or 45° such that the freestream velocity is $\vec{U}_\infty = (U_\infty \cos\Lambda,\ 0,\ U_\infty \sin\Lambda)$. For the swept case, coordinates (x', y, z') are formed by rotating the base (x, y, z) coordinates by Λ to align x' with the freestream direction. The velocity components associated with the base Cartesian coordinates are (u, v, w), while $(u_\Lambda, v, w_\Lambda)$ denote the velocities in the crossflow (x', y, z') coordinates. The Reynolds number based on the momentum thickness at the inlet, θ_0, is $Re_{\theta_0} = 790$, such that by $x/L = -0.6$, the TBL thickness is approximately $h/8$ with $Re_\theta \approx 1050$, matching experiments and previous DNS (Williams et al., 2020; Balin and Jansen, 2021).

Special consideration is required for the top boundary condition to model the confinement induced by the boundary layer growth on the top wall of the experimental wind tunnel. Due to limited information on the top-wall boundary layer development, we apply the general 1/7th power law to prescribe the displacement thickness δ^* as a function of θ_0 and the streamwise distance from the inlet $(x - x_0)$:

$$\frac{\delta^*}{\theta_0} = \frac{0.046}{Re_{\theta_0}} \left[\left(\frac{x - x_0}{\theta_0} \right) Re_{\theta_0} + \left(\frac{Re_{\theta_0}}{0.0363} \right)^{\frac{5}{4}} \right]^{\frac{4}{5}} \tag{2}$$

The top wall at $y/L \approx 0.5$ is tilted according to the above expression and treated with a slip wall condition. Although this approach assumes unobstructed boundary-layer growth, which is not strictly true due to the presence of the bump, it avoids the uncertainty of RANS-based boundary conditions used in previous DNS (Balin and Jansen, 2021; Shur et al., 2021).

The mesh is of DNS quality with average spacings of $\Delta_x^+ = 10$ and $\Delta_z^+ = 5$, with a first off-wall point at $y^+ = 0.1$ and 24 points in $y^+ < 10$ (+ superscripts indicate wall units). The total number of spectral elements is approximately 3.2 million, resulting in approximately 1.6 billion grid points using 7th-order spatial polynomials. The flow was simulated for 1.5 flow-through times (FTT) to remove initial transients, before collecting statistics for an additional 5.6 FTT, which are also averaged in the z direction.

RESULTS

Figure 2 displays contours of the instantaneous x velocity (u) on a z slice of the unswept and swept flow fields. The overall u velocity is lower in the swept case since the freestream

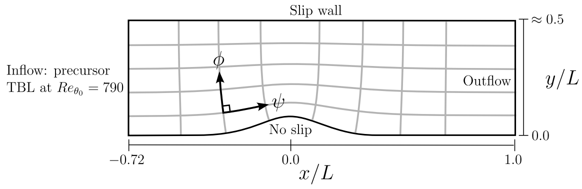

Figure 1. A schematic of a streamwise cross-section of the computational domain, showing the SCS and boundary conditions.

velocity in the x-direction is $U_\infty/\sqrt{2}$. The boundary layer is visibly thicker on the leeward side of the bump in the swept case, with a larger degree of x backflow ($u < 0$, cyan) in figure 2b compared to the small regions of incipient separation observed for the unswept bump in figure 2a. In the mean, the incipient separation for the unswept bump appears as a small separated region, as in past DNS at the same Re_L (Uzun and Malik, 2021; Balin and Jansen, 2021; Shur et al., 2021).

Unswept (Baseline) Configuration

The development of the mean pressure coefficient, $C_p = (P - P_{\text{ref}})/\frac{1}{2}\rho U_\infty^2$, and the skin friction coefficient, $C_f = \tau_w/\frac{1}{2}\rho U_\infty^2$, along the bottom wall for the unswept case are compared to published DNS data at $Re_L = 1$ million in figure 3. In the above expressions, ρ is the fluid density and τ_w is the wall shear stress, while the reference pressure, P_{ref}, is taken such that $C_p = 0$ on the wall at $x/L = -0.6$ (Balin and Jansen, 2021). Figure 3a shows reasonable agreement in C_p between the DNS results, besides small differences at the bump peak and a lower C_p of Balin and Jansen (2021) downstream of the bump, most likely due to differences in confinement. In terms of the skin friction, figure 3b shows a similar peak in C_f as Uzun and Malik (2021) and Shur et al. (2021), with a second peak downstream of the top of the bump closer to that of Shur et al. (2021) than Uzun and Malik (2021) or Balin and Jansen (2021). This second peak in C_f is strongly dependent on the relaminarization of the TBL. In particular, Shur et al. (2021) found a link between larger numerical dissipation and a smaller second C_f peak and weaker separation extent, which provides confidence in the present results. As mentioned in the discussion of the instantaneous flow, the incipient separation on the leeward side of the bump appears as a small region of slightly negative C_f near $x/L = 0.2$.

In analyzing the flow over the unswept bump, we make use of the streamline coordinate system (SCS) proposed by Finnigan (1983), which consists of orthogonal coordinates following mean streamlines (ψ) and streamwise-normal lines (ϕ), as depicted in figure 1. The third orthogonal coordinate is z, arising from the homogeneous direction of the mean flow. The plotted ψ and ϕ lines in figure 1 demonstrate the orthogonality of the coordinates, as well as the way in which the ϕ coordinate curves to become normal to both the wall and the freestream velocity. Away from the hump on the flat plate, the ϕ lines appear nearly vertical. The SCS represents a Frenet–Serret (TNB) basis, which was recently extended to complex-lamellar three-dimensional flows by Finnigan (2024). The benefits of the SCS are that it naturally follows the mean flow and underlying geometry, greatly simplifying and making more interpretable the governing equations, which explicitly contain curvature and streamwise acceleration terms in the SCS form. In the irrotational flow outside the boundary layer, ϕ becomes equivalent to potential lines, while ψ are stream-

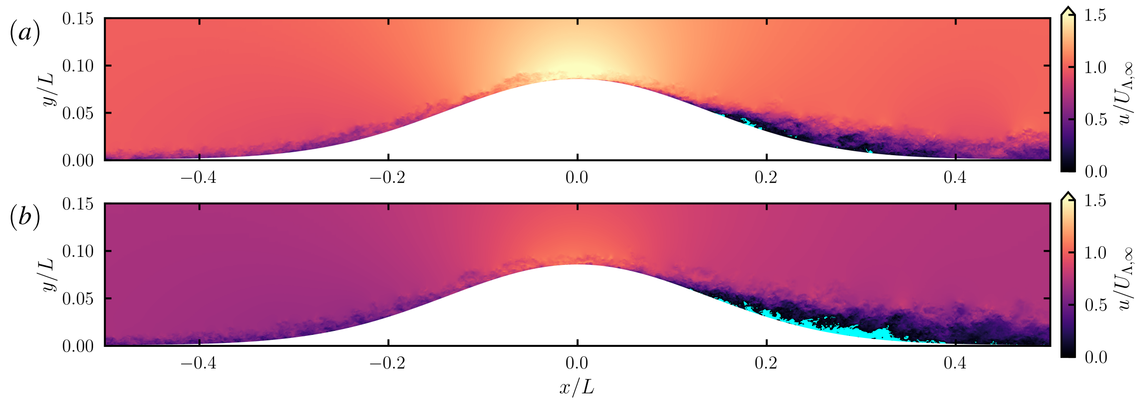

Figure 2. Instantaneous contours of x velocity for the unswept case (a), and the swept case (b). Values $u < 0$ are colored in cyan.

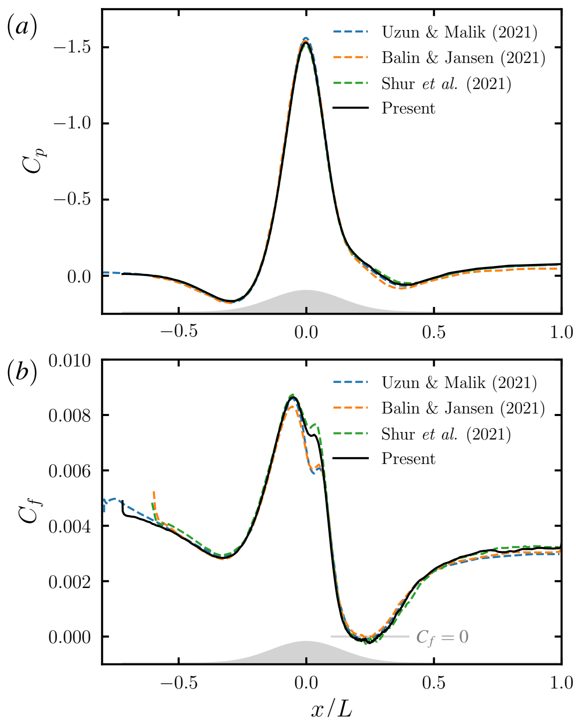

Figure 3. Mean pressure coefficient (a) and skin friction coefficient (b) along the bottom wall compared to published DNS results for the unswept bump at $Re_L = 1$ million.

lines, providing a strong link to potential flow theory.

As stated above, the SCS has already been used to analyze the mean momentum balance (MMB) on the windward side of the bump at $Re_L = 2$ million (Prakash et al., 2024), as well as a thick axisymmetric TBL (Morse and Mahesh, 2021). Recently, Patton et al. (2026) used the SCS to study turbulence production over isolated forested hills, which bear similarities to the flow considered here. The SCS has also been used successfully in the study of turbulence near surface waves (Yousefi and Veron, 2020; Xuan and Shen, 2022).

In the flat-plate, near zero pressure gradient (ZPG) flow near the inflow boundary, the profiles in the SCS agree closely with profiles in standard Cartesian coordinates, despite a small rotation due to the non-zero mean vertical velocity, V. Figure 4 shows mean velocity magnitude and Reynolds stress profiles along a ϕ line originating from the wall at $x/L \approx -0.64$, compared with the ZPG TBL data of Schlatter and Örlü (2010) at similar local Reynolds numbers, showing good agreement.

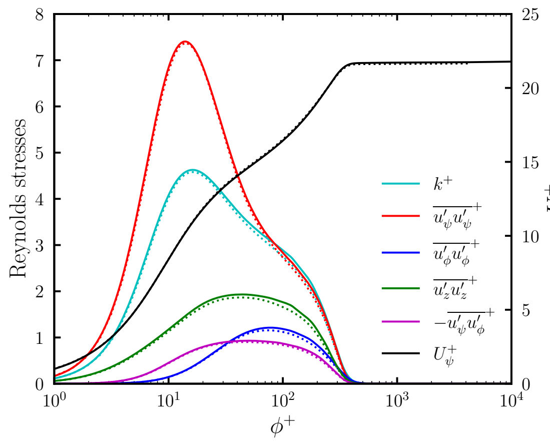

Figure 4. Mean velocity and Reynolds stress profiles near the inlet at $x/L \approx -0.64L$ (solid lines, $Re_\theta \approx 931$, $Re_\tau \approx 344$) compared to the reference ZPG TBL data of Schlatter and Örlü (2010) (dotted lines, $Re_\theta = 1000$, $Re_\tau = 360$).

In figure 5b, we show profiles of mean velocity and Reynolds stresses on a ϕ line ahead of the bump apex, originating from $x/L \approx -0.05$, as drawn in figure 5a. In this region, the favorable pressure gradient approaching the bump apex has nearly eliminated the mean velocity gradient in the outer layer, reducing the overall momentum thickness of the boundary layer. The $\overline{u_\psi'^2}$ Reynolds stress is reduced by around 10% compared to the ZPGTBL in inner units, resulting in a corresponding reduction in the turbulent kinetic energy (TKE, $k = \frac{1}{2}\overline{u_i' u_i'}$). The other Reynolds stresses are even more greatly reduced. It is also near this station where the Reynolds shear stress reaches its minimum value in inner units, as shown using profiles from multiple ϕ lines in figure 5c.

In the SCS, the mean momentum balance (MMB) under the boundary layer approximation takes the form

$$\overbrace{U_\psi \frac{\partial U_\psi}{\partial \psi}}^{\mathrm{MI}_\psi} = \overbrace{-\frac{1}{\rho}\frac{\partial P}{\partial \psi}}^{\mathrm{PG}_\psi} + \left[\overbrace{\frac{\partial}{\partial \phi}\left(-\overline{u_\psi' u_\phi'}\right)}^{\mathrm{TI}_\psi} + \overbrace{\nu \frac{\partial^2 U_\psi}{\partial \phi^2}}^{\mathrm{VF}_\psi} \right] \tag{3}$$

$$\underbrace{\frac{U_\psi^2}{R_\psi}}_{\mathrm{CF}_\phi} = \underbrace{-\frac{1}{\rho}\frac{\partial P}{\partial \phi}}_{\mathrm{PG}_\phi} + \underbrace{\frac{\partial}{\partial \phi}\left(-\overline{u_\phi'^2}\right)}_{\mathrm{TI}_\phi} \tag{4}$$

where we note that partial derivatives from the traditional

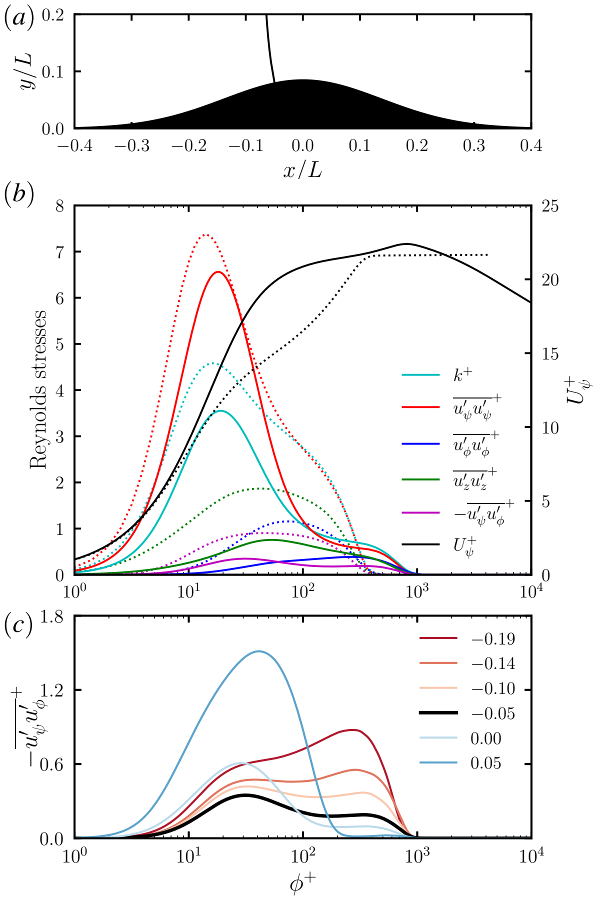

Figure 5. Mean velocity and Reynolds stress profiles (panel *b*) for the unswept case (solid lines, $Re_\theta \approx 689$, $Re_\tau \approx 641$) on the windward side of the bump on a ϕ line originating at $x/L \approx -0.05$, shown in panel *a*. The reference ZPGTBL data of Schlatter and Örlü (2010) (dotted lines, $Re_\theta = 1000$, $Re_\tau = 360$) is also shown. Panel *c* shows $-\overline{u_\psi' u_\phi'}$ on multiple ϕ lines, with approximate x/L positions shown in the legend.

MMB are replaced by directional derivatives in the SCS, such that derivatives of vector/tensoral quantities include contributions from coordinate rotation. Specifically, directional derivatives of the Reynolds stress tensor ($\overline{u_i' u_j'}$) differ from locally-aligned partial derivatives due to contributions from coordinate rotation along ψ and ϕ lines. The above equations now directly include the local streamline curvature, defined by $\frac{1}{R_\psi} = \frac{1}{U_\psi}\left(\Omega + \frac{\partial U_s}{\partial \phi}\right)$, where Ω is the spanwise mean vorticity ($R_\psi^{-1} > 0$ for concave curvature). While R_ψ^{-1} defines the curvature of the streamlines (ψ), a similar curvature $\frac{1}{L_a} = \frac{1}{U_\psi}\frac{\partial U_\psi}{\partial \psi}$ describes the curvature of streamwise-normal (ϕ) coordinate lines. This L_a^{-1} curvature is related to the *e*-folding length scale of streamwise acceleration (Finnigan, 1983).

Figure 6 shows contours of these mean curvatures R_ψ^{-1} and L_a^{-1} over the bump, along with black contour lines indicating their inflection points. Figure 6*a* illustrates the concave curvature ($R_\psi^{-1} > 0$) upstream of the inflection point of the Gaussian wall surface curvature ($x/L \approx -0.1379$, Uzun and Malik (2021)), from which the curvature inflection line extends nearly straight from the wall. This is in contrast to the thick axisymmetric TBL of Morse and Mahesh (2021), in which the inflection line was strongly misaligned with the wall normal, suggesting that wall-aligned coordinates are more adequate for this flow. After the inflection line, the convex curvature ($R_\psi^{-1} < 0$) over the bump apex reaches a larger magnitude than the peak concave curvature at $x/L \approx -0.25$, consistent with the magnitude of the wall curvature (Uzun and Malik, 2021). L_a^{-1} in figure 6*b* illustrates the strong flow acceleration from $x/L \approx -0.3$ until the bump apex, which is concentrated near the wall. The inflection line of L_a^{-1} extends nearly vertically away from the bump apex, but reaches in the upstream direction near the wall toward $x/L \approx -0.05$ (marked in figure 6*b*). It is near this $x/L \approx -0.05$ station that the peak of $-\overline{u_\psi' u_\phi'}^+$ reaches its minimum (figure 5*c*) and the favorable streamwise pressure gradient begins to rapidly decrease, leading to a net streamwise deceleration near the wall.

Figure 7*a* displays the streamwise (ψ) MMB on the same ϕ line shown in figure 5*a*. At this station, the PG_ψ term is still elevated at the wall (FPG, $\partial P/\partial \psi < 0$), resulting in $\mathrm{MI}_\psi > 0$. However, after this station, PG_ψ drops rapidly such that MI_ψ develops a negative peak before the bump apex, reflecting the observations from figure 6*b*. Figure 7*b* shows the streamwise-normal (ϕ) MMB at the same station, where the centripetal acceleration, $\mathrm{CF}_\phi = U_\psi^2/R_\psi$, dominates the normal pressure gradient above the buffer layer. Outside the boundary layer, the viscous and turbulent stresses in equations 3 and 4 disappear, and we are left with statements of potential flow: Bernoulli's equation along streamlines ($\mathrm{MI}_\psi = \mathrm{PG}_\psi$) and Euler's equation normal to them ($\mathrm{CF}_\phi = \mathrm{PG}_\phi$) in figure 7*a*, *b*.

Additional SCS expressions can also be constructed for budgets of $-\overline{u_\psi' u_\phi'}$ and k (Finnigan, 1983). The convection and production terms of the k budget are

$$\overbrace{U_\psi \frac{\partial k}{\partial \psi}}^{C} = \overbrace{\left(\overline{u_\phi'^2} - \overline{u_\psi'^2}\right)\frac{\partial U_\psi}{\partial \psi}}^{P^E} \overbrace{-\overline{u_\psi' u_\phi'}\left(\frac{\partial U_\psi}{\partial \phi} + \frac{U_\psi}{R_\psi}\right)}^{P^S} + \dots \quad (5)$$

where the total production is $P = P^E + P^S$ and we have left out the dissipation (ε) and turbulent (T), pressure (Π), and viscous (D) transport terms on the right-hand side (RHS). The first term on the RHS (P^E) is the production via the streamwise extensional strain, while the second term (P^S) is production via shear, which is affected by a curvature term, U_ψ/R_ψ. This shear also appears in the decomposition of the mean vorticity into rigid body rotation and shear components as $\Omega = \left(2\frac{U_\psi}{R_\psi}\right) - \left(\frac{\partial U_\psi}{\partial \phi} + \frac{U_\psi}{R_\psi}\right) = \Omega_{\mathrm{rot}} - \Omega_{\mathrm{shear}}$, where the shear component appears in the mean strain rate tensor through $S_{11} = -S_{22} = \frac{\partial U_\psi}{\partial \psi}$, $S_{12} = S_{21} = \Omega_{\mathrm{shear}}/2$. The fact that the TKE production depends explicitly on S_{ij} is well-known, and while the streamline curvature does appear in the TKE budget, it only affects production indirectly by modification of S_{ij}.

In contrast, a more explicit curvature effect does appear in the $-\overline{u_\psi' u_\phi'}$ budget, given by

$$\overbrace{U_\psi \frac{\partial\left(-\overline{u_\psi' u_\phi'}\right)}{\partial \psi}}^{C_{\psi\phi}} = \overbrace{\overline{u_\phi'^2}\frac{\partial U_\psi}{\partial \phi}}^{P^G_{\psi\phi}} + \overbrace{\overline{u_\psi'^2}\frac{U_\psi}{R_\psi}}^{P^C_{\psi\phi}} + \overbrace{\left(\overline{u_\psi'^2} - \overline{u_\phi'^2}\right)\frac{U_\psi}{R_\psi}}^{P^P_{\psi\phi}} + \dots \quad (6)$$

where we have again omitted the $\varepsilon_{\psi\phi}$, $T_{\psi\phi}$, $\Pi_{\psi\phi}$, and $D_{\psi\phi}$ terms for brevity, and the total production is $P_{\psi\phi} = P^G_{\psi\phi} + P^C_{\psi\phi} + P^P_{\psi\phi}$. The $P^G_{\psi\phi}$ term is the traditional generation via the velocity gradient normal to the mean flow, while the second term, $P^C_{\psi\phi}$, is related to the buoyancy production analogy of Bradshaw (1969) for streamline curvature. This term is posi-

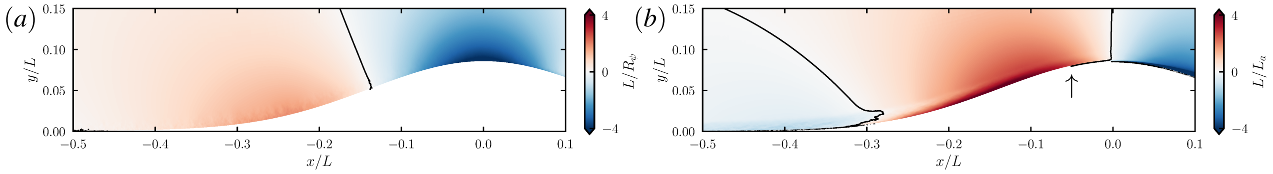

Figure 6. Contours of L/R_ψ (a) and L/L_a (b) for the unswept case. A contour line for the zero level is shown in black for each case.

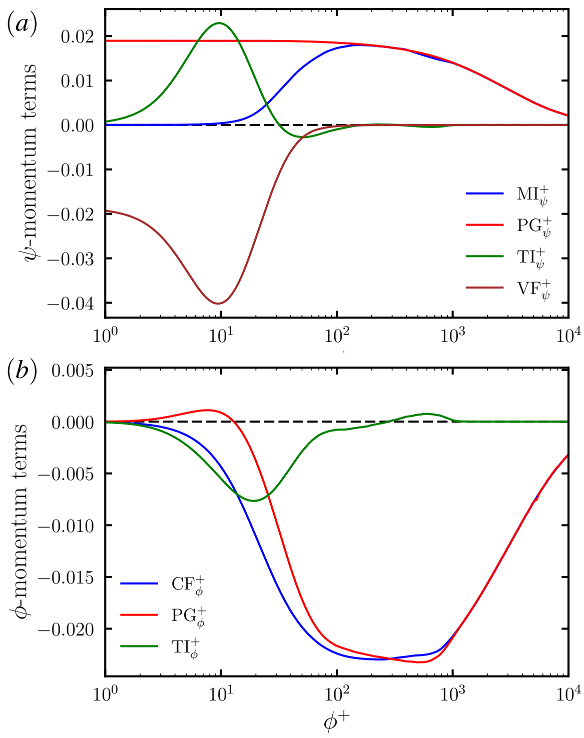

Figure 7. MMB for the unswept case in the ψ (a) and ϕ (b) directions for the ϕ line shown in figure 5a.

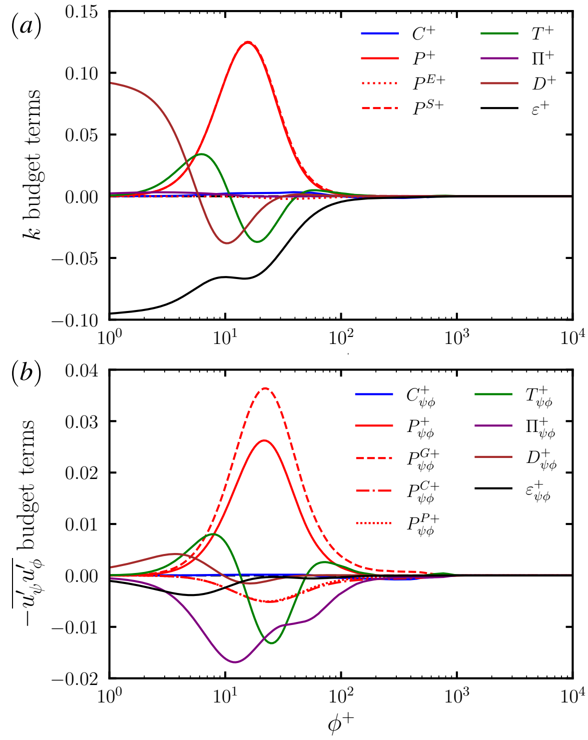

Figure 8. Inner-scaled budgets of k (a) and $\overline{u'_\psi u'_\phi}$ (b) for the ϕ line shown in figure 5a.

tive in the concave curvature at the front of the bump and negative in the convex curvature over the its peak (figure 6a). The final term on the RHS, $P^P_{\psi\phi}$, is the "pseudo" production due to the rotation of the coordinate axes along ψ (Xuan and Shen, 2022). This same term is also contained within the directional derivative in the convection term ($C_{\psi\phi}$) on the left-hand side.

Figure 8 shows the budgets of TKE and $-\overline{u'_\psi u'_\phi}$ on the same ϕ line as in the MMB discussion. The TKE budget appears as expected, with the shear production dominating the extensional component (this is also reflected in the $\overline{u'^2_\psi}$ budget, not shown). While the curvature term (U_ψ/R_ψ) in the shear rate is negative over the top of the bump (figure 6a), acting to lower P^S, its effect on the near-wall production peak is negligible compared to the streamwise-normal velocity gradient. However, it does have a larger influence on the outer layer production, where it, combined with the P^E, decreases the total production to near zero. In the budget for $-\overline{u'_\psi u'_\phi}$, the effect of the curvature on the production peak is much more pronounced, with the $P^C_{\psi\phi} + P^P_{\psi\phi}$ terms combining to reduce the peak $P_{\psi\phi}$ by nearly 30% below the gradient contribution of $P^G_{\psi\phi}$. The production in the outer layer is also reduced to near zero. A result of the attenuated $-\overline{u'_\psi u'_\phi}$ is a reduction of P^S in the TKE budget, via an indirect curvature effect.

Swept Configuration

Finally, we turn to the flow over the bump in the swept configuration ($\Lambda = 45°$), for which we observed a larger degree of backflow than the unswept flow in figure 2. To investigate this in greater detail, we examine the flow over the bump in the (x', y, z') coordinates aligned with the freestream velocity, where x' points in the direction of $\vec{U}_\infty$. The associated instantaneous velocities in this frame are $(u_\Lambda,\ v,\ w_\Lambda)$. Figure 9 displays instantaneous contours of u_Λ and w_Λ, where we do not observe any region of $u_\Lambda < 0$ as was present in u contours in figure 2b. As the flow approaches the bump, figure 9b shows that w_Λ becomes slightly positive in the due to the APG imposed by the bump. This switches to a FPG approaching the bump apex, resulting in a strong negative w_Λ velocity, which acts as a secondary velocity component to create a skewing of the overall velocity profile, forming a strong 3DTBL effect. In the APG on the leeward side of the bump, w_Λ switches back to large positive values past $x/L = 0.1$ within the boundary layer. This in turn contributes to the negative u velocity observed in figure 2b, based on the projection of w_Λ to the x axis as $-w_\Lambda \sin\Lambda$. For the region outside the boundary layer for $x/L > 0$, there is no such shift to positive w_Λ. The resulting mean flow topology on the leeward side of the bump consists of a separation region with a strong z velocity component.

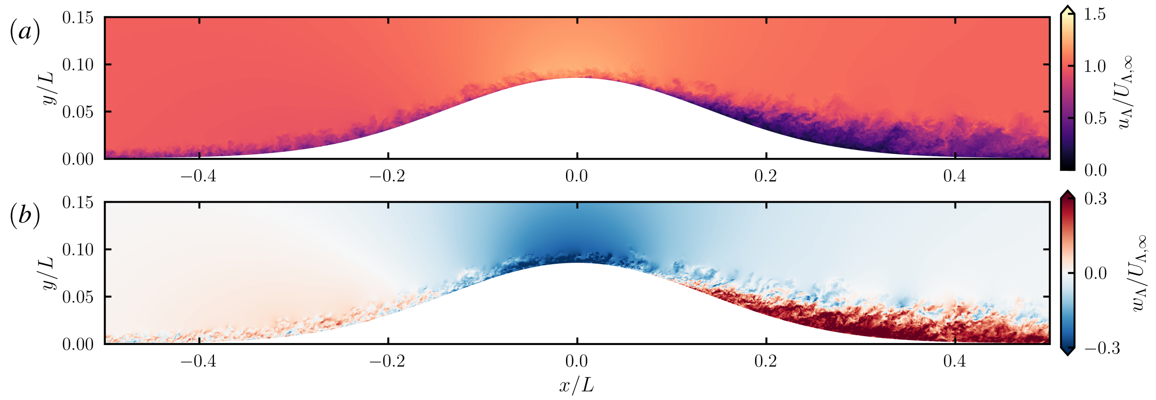

Figure 9. Instantaneous contours of u_Λ (a) and w_Λ (b) velocity components for the swept case, where there is no region where $u_\Lambda < 0$.

CONCLUSIONS

We presented DNS results of flow over the Boeing Gaussian bump at $Re_L = 1$ million for an unswept configuration and, for the first time, for a 45° swept flow. The two configurations exhibit significant structural differences on the leeward side of the bump, with a three-dimensional separated flow in the swept case, compared to incipient separation in the baseline case. For the swept case, the pressure gradients over the bump lead to a significant three-dimensionality of the flow over the bump apex, with a sudden inversion of the crossflow velocity on the leeward side. For the unswept case, streamline coordinate analysis of the mean momentum balance and, for the first time, turbulence budgets illustrated the direct and indirect effects of streamline curvature. Specifically, curvature effects appear indirectly in the TKE production via a small near-wall contribution to the shear rate. However, the curvature effect much more strongly reduces the Reynolds shear stress production, which indirectly affects TKE production. Hence, we presented for the first time the quantified effect of streamline curvature on turbulent stresses for the Boeing bump TBL. Finally, observations of the streamwise acceleration length scale revealed that its inversion starts near the wall ahead of the bump apex, approximately coinciding with the station where the inner-scaled peak of the TKE and Reynolds shear stress start to recover as the favorable pressure gradient diminishes.

ACKNOWLEDGMENTS

This work was funded by the Swedish Research Council (Vetenskapsrådet) through the “The Boeing hump – turbulent separated flow with sweep ” project (2022-04226_VR).

REFERENCES

Balin, R. and Jansen, K.E. 2021 Direct numerical simulation of a turbulent boundary layer over a bump with strong pressure gradients. *Journal of Fluid Mechanics* **918**, A14.

Bradshaw, P. 1969 The analogy between streamline curvature and buoyancy in turbulent shear flow. *Journal of Fluid Mechanics* **36** (1), 177–191.

Finnigan, J.J. 1983 A streamline coordinate system for distorted two-dimensional shear flows. *Journal of Fluid Mechanics* **130**, 241–258.

Finnigan, J.J. 2024 Streamline coordinates in three-dimensional turbulent flows. *Journal of Fluid Mechanics* **999**, A101.

Fischer, P.F., Lottes, J.W. and Kerkemeier, S.G. 2008 Nek5000 Web page. https://nek5000.mcs.anl.gov.

Lozano-Durán, A., Giometto, M.G., Park, G.I. and Moin, P. 2020 Non-equilibrium three-dimensional boundary layers at moderate Reynolds numbers. *Journal of Fluid Mechanics* **883**, A20.

Morse, N. and Mahesh, K. 2021 Large-eddy simulation and streamline coordinate analysis of flow over an axisymmetric hull. *Journal of Fluid Mechanics* **926**, A18.

Patton, Edward G., Finnigan, J. J., Harman, I. N. and Sullivan, P. P. 2026 Turbulent flow over isolated forested hills of varying shape and steepness. *Journal of Fluid Mechanics* **1026**, A16.

Prakash, A., Balin, R., Evans, J.A. and Jansen, K.E. 2024 A streamline coordinate analysis of a turbulent boundary layer subject to pressure gradients and curvature on the windward side of a bump. *Journal of Fluid Mechanics* **984**.

Schlatter, P. and Örlü, R. 2010 Assessment of direct numerical simulation data of turbulent boundary layers. *Journal of Fluid Mechanics* **659**, 116–126.

Shur, M.L., Spalart, P.R., Strelets, M.Kh. and Travin, A.K. 2021 Direct numerical simulation of the two-dimensional speed bump flow at increasing Reynolds numbers. *International Journal of Heat and Fluid Flow* **90**.

Slotnick, J.P. 2019 Integrated CFD validation experiments for prediction of turbulent separated flows for subsonic transport aircraft. *Tech. Rep.* STO-MP-AVT-307. NATO Science and Technology Organization.

Uzun, A. and Malik, M.R. 2021 Simulation of a turbulent flow subjected to favorable and adverse pressure gradients. *Theoretical and Computational Fluid Dynamics* **35**, 293–329.

Uzun, A. and Malik, M.R. 2022 High-fidelity simulation of turbulent flow past Gaussian bump. *AIAA Journal* **60**, 2130–2149.

Uzun, A. and Malik, M.R. 2025 Direct numerical simulation of flow past a Gaussian bump at a high Reynolds number. In *AIAA SCITECH 2025 Forum*, p. 0060.

Williams, O., Samuell, M., Sarwas, E.S., Robbins, M. and Ferrante, A. 2020 Experimental study of a CFD validation test case for turbulent separated flows. In *AIAA Scitech 2020 Forum*, p. 0092.

Xuan, A. and Shen, L. 2022 Analyses of wave-phase variation of Reynolds shear stress underneath surface wave using streamline coordinates. *Journal of Fluid Mechanics* **931**, A32.

Yousefi, K. and Veron, F. 2020 Boundary layer formulations in orthogonal curvilinear coordinates for flow over wind-generated surface waves. *Journal of Fluid Mechanics* **888**, A11.